CHIN. PHYS. LETT. Vol. 38, No. 3 (2021) 036301

Quantum Transport across Amorphous-Crystalline Interfaces in Tunnel Oxide Passivated Contact Solar Cells: Direct versus Defect-Assisted Tunneling

Feng Li(李峰)[1,2*], Weiyuan Duan(端伟元)[2], Manuel Pomaska[2], Malte Köhler[2], Kaining Ding(丁凯宁)[2], Yong Pu(普勇)[1*], Urs Aeberhard[2], and Uwe Rau[2]

[1]*College of Science, Nanjing University of Posts and Telecommunications, Nanjing 210023, China*
[2]*IEK-5 Photovoltaik, Forschungszentrum Jülich, 52425 Jülich, Germany*

(Received 24 October 2020; accepted 9 December 2020; published online 2 March 2021)

Tunnel oxide passivated contact solar cells have evolved into one of the most promising silicon solar cell concepts of the past decade, achieving a record efficiency of 25%. We study the transport mechanisms of realistic tunnel oxide structures, as encountered in tunnel oxide passivating contact (TOPCon) solar cells. Tunneling transport is affected by various factors, including oxide layer thickness, hydrogen passivation, and oxygen vacancies. When the thickness of the tunnel oxide layer increases, a faster decline of conductivity is obtained computationally than that observed experimentally. Direct tunneling seems not to explain the transport characteristics of tunnel oxide contacts. Indeed, it can be shown that recombination of multiple oxygen defects in a-SiO_x can generate atomic silicon nanowires in the tunnel layer. Accordingly, new and energetically favorable transmission channels are generated, which dramatically increase the total current, and could provide an explanation for our experimental results. Our work proves that hydrogenated silicon oxide (SiO_x:H) facilitates high-quality passivation, and features good electrical conductivity, making it a promising hydrogenation material for TOPCon solar cells. By carefully selecting the experimental conditions for tuning the SiO_x:H layer, we anticipate the simultaneous achievement of high open-circuit voltage and low contact resistance.

DOI: 10.1088/0256-307X/38/3/036301

Passivating and carrier-selective contacts count among the key elements to further increase the efficiency of silicon-based solar cells. One of the main representatives of device architectures implementing such contacts is the tunnel-oxide passivated contact (TOPCon) solar cell, consisting of an ultrathin amorphous SiO_x (a-SiO_x) layer on an Si wafer, in combination with a heavily doped silicon film.[1] TOPCon solar cells have undergone rapid development in the past decade. By applying TOPCons as a full-area rear contacts, a record efficiency of more than 25% could be achieved for an area of $2\times2\,\mathrm{cm}^2$,[2] and more than 21% for areas larger than $100\,\mathrm{cm}^2$.[3,4] Careful engineering is key to the achievement of high efficiency: (1) high quality interface passivation of the tunnel oxide layer (long carrier lifetime), (2) efficient doped layers in c-Si (high V_{oc}) and (3) efficient majority carrier transport (high fill factors).

While several new materials for passivated contacts besides a-SiO_x have been reported, e.g., a-SiC,[5] a-SiO_x is the most widely used, as it exhibits extraordinary characteristics as an effective buffer layer, combining several beneficial properties: it is anticipated not only to effectively reduce recombination and lower production costs (withstanding industrial contact firing) but also to reduce optical losses.[6] Due to the wide bandgap of a-SiO_x, band-like electronic transport is suppressed, and tunneling becomes the main transport mechanism when the thickness of the oxide layer is at the nanometer level.[7] In this respect, the transport processes at a-SiO_x passivated contacts differ from those at the classical a-Si:H passivated contact in silicon heterojunction devices, where a significant fraction of the current is assumed to be thermally activated.[8] In spite of the critical role of the oxide barrier, a microscopic understanding of the relation between local electronic structure (in terms of nanoscale thickness fluctuations, defect states, etc.) and the transmission characteristics of the oxide barrier is currently lacking.

In order to narrow this gap in understanding, we explore the electronic properties of a-SiO_2 and a-SiO_x passivating contacts, as used in the TOPCon solar cell architecture, from a microscopic perspective. We first compute the atomic configuration and electronic structure of c-Si, a-SiO_2 and a-SiO_x, respectively, based on first principles calculations. Next, by coupling the Hamiltonians of the different materials, a sandwich structure of c-Si/a-SiO_x/c–Si is constructed, using the lead-conductor-lead (LCR) model[9,10] in an open boundary condition. For this contacted sandwich structure, the tunneling transport properties are analyzed based on an integrated approach, combining the density functional theory (DFT) with a non-equilibrium Green's function picture of ballistic quantum transport. One significant finding is that the

Supported by the National Natural Science Foundation of China (Grant Nos. 61704083 and 61874060), the Natural Science Foundation of Jiangsu Province (Grant No. BK20181388), and NUPTSF (Grant No. NY219030).
*Corresponding authors. Email: lifeng@njupt.edu.cn; puyong@njupt.edu.cn
© 2021 Chinese Physical Society and IOP Publishing Ltd

transport across the tunnel oxide layer depends not only on the passivation and the thickness of the barrier layer, but also on the presence and configuration of *oxygen defects in* a-SiO_x. In the case of multiple defects, these were found to recombine, forming a type of atomic silicon nanowires in the a-SiO_x layer, due to structural reorganization. The presence of such "monofilament pinholes" significantly enhances conductance as new transmission channels are opened.

Methods. We computed the electronic transport property of c-Si/a-SiO_x:H/c-Si sandwich structures by using an integrated approach, combining the DFT with non-equilibrium Green's function formalism (NEGF). Similar approaches have been used to assess leakage currents in gate oxides.[8] In the first step, an *ab initio* molecular dynamic simulation (AIMD) was performed to build the structures of a-SiO_2 and c-Si/a-SiO_x:H/c-Si, using tools from the VASP package.[11,12] Next, the Hamiltonian matrix was obtained, based on static electronic computation, using the PWSCF code available in the Quantum ESPRESSO suite.[13] Here, $10\times10\times10$, $4\times4\times4$ and $2\times2\times1$ Monkhorst-Pack k-point grids were considered for the Brillouin zones of c-Si, a-SiO_2, and c-Si/a-SiO_x:H/c-Si, respectively. A cutoff energy of 450 eV for the wavefunctions provided a converged electronic density of states. The convergence of energy and force were set at 10^{-6} eV and 0.001 eV/Å, respectively.

We then used the maximally localized Wannier functions (MLWFs), together with the Landauer formula[14] as implemented in the WanT code,[15] to compute the total conductance in the lead-conductor-lead (LCR) model. The computational details are described in the Supplementary Materials.

Results and Discussion—c-Si/a-SiO₂:H/c-Si. Constructing the geometric structure at the amorphous-crystalline interface represents a starting point from which to examine the impact of interfacial properties on device characteristics. The microscopic picture of the complex interface region is captured by means of an *ab initio* description, allowing for a comprehensive assessment of the device-relevant states. In order to construct the relevant structural model, a-SiO_2 is inserted as a tunnel oxide layer between crystalline silicon layers, resulting in a c-Si/a-SiO_2:H/c-Si sandwich structure.

We first consider the structural, electronic and transport properties of ideal bulk c-Si, in order to verify the correctness of the integrated simulation approach. To achieve a linear scaling of required computing time, the electron Bloch wavefunctions obtained from the *ab initio* calculation are translated into MLWF forms by means of a unitary transformation. The computed electronic band structure and transmission gap of c-Si are shown in Figs. S1 and S2 in the Supplementary Materials. We observe a clear indirect bandgap of 0.60 eV, which is very close to the DFT result of 0.61 eV. The band edges around the Fermi level of c-Si are also provided, via the analysis of the layer-resolved density of states (LRDOS, Fig. S2). This result proves that the MLWFs method conserves the accuracy of the first-principles electronic structure calculations, confirming the reliability of the integrated method used in this work. We therefore used atomic orbitals as the initial Wannier functions for MLWFs in all of our computations.

The efficiency of charge carrier extraction across tunnel oxide barriers depends on a range of configurational parameters, including (a) tunnel oxide layer thickness, (b) interfacial passivation, and (c) oxygen defects in a-SiO_x:H (i.e., the stoichiometry of the oxide). In view of their potential impact on solar cell efficiency, we will discuss these factors below, both individually and from a microscopic perspective.

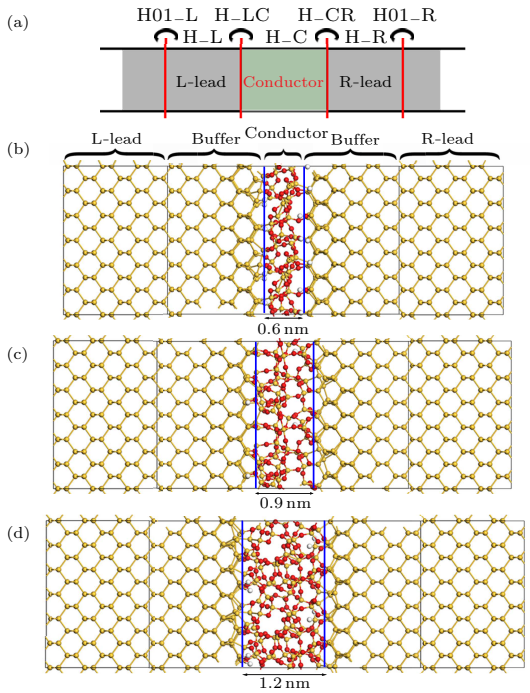

Fig. 1. (a) Schematic representation of the lead-conductor-lead (LCR) model. Fully optimized geometric structures of three cases, in which the thicknesses of a-SiO_2 layers are (b) 0.6, (c) 0.9 and (d) 1.2 nm. Here c-Si layers of ∼1.6 nm thickness are inserted between the central oxide layer and the leads in order to release the local stress at the interfaces.

Role of Tunnel Oxide Layer Thickness. In the TOPCon solar cell fabrication process, precise control of the thickness of the a-SiO_2 tunnel oxide layer is challenging. In this situation, it is to be expected that the fluctuation of a-SiO_2 layer thickness will affect electronic transport across the amorphous-crystalline interfaces (Fig. S3). The effect of tunnel oxide layer thickness becomes even more critical when the thickness of the a-SiO_2 layer is as small as only a few nanometers, since the geometric and electronic properties of thinner buffer layers are more readily affected by the substrate. As shown in Fig. 1, three different thicknesses of a-SiO_2 layers are investigated in this work: 0.6, 0.9, and 1.2 nm, respectively, which are

close to the experimentally estimated ideal thickness of ∼1 nm.[16] To fully release the local stress at the interfaces, two additional c-Si buffer layers with a thickness of 1.6 nm are inserted between the central a-SiO_2 layer and the c-Si leads. Since oxygen has a much higher electronegativity (3.4) than silicon (1.9), the original surface of Si (100) will be seriously modified after full optimization, leaving some interfacial silicon atoms with dangling bonds. To passivate these defects, H atoms are used to saturate all the dangling bonds.

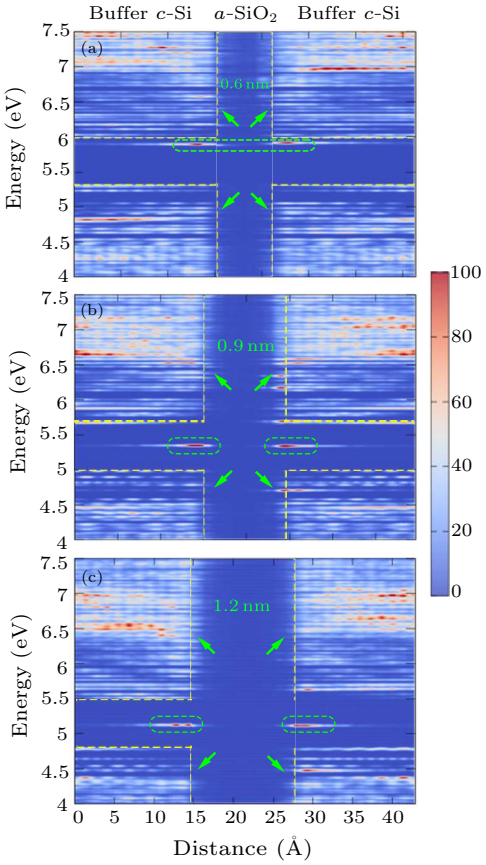

Fig. 2. Layer-resolved density of states (LRDOS) of the c-Si/a-SiO_2:H/c-Si sandwich structure, with a-SiO_2 tunnel oxide layer thicknesses of (a) 0.6 nm, (b) 0.9 nm and (c) 1.2 nm. The continuous transmission channels across the tunnel oxide layer rapidly disappear when the width of the a-SiO_2 layer increases from 0.6 nm to 1.2 nm.

As transport requires the availability of current-carrying states at the relevant energies close to the band edges of the contact materials, we computed and analyzed the LRDOS for the c-Si/a-SiO_2:H/c-Si structure, as shown in Fig. 2. The slight asymmetry of band structure is due to the dissymmetry of interfacial geometric structures. In order to compare the energy levels between the different cases, the valence and conduction band positions are evaluated based on the model-solid theory,[17] in which the average of the electrostatic potential is defined as the reference level. The computational details of the model-solid theory are given in Fig. S1. The positions determined in this way amount to 5.32 eV (0.6 nm), 5.00 eV (0.9 nm) and 4.82 eV (1.2 nm) for the VBM, and to 5.95 eV (0.6 nm), 5.68 eV (0.9 nm) and 5.46 eV (1.2 nm) for the CBM. In Fig. 2, these positions are highlighted by yellow dashed lines. The downshift in VBM and CBM as a function of the oxide layer thickness is attributed to the increase in the proportion of oxygen.

Based on the LRDOS image, we found that some local density of states is formed at the interfaces of c-Si/a-SiO_2. According to their characteristics, the associated states can be divided into two groups: one group consists of strongly localized states, as enclosed by the green circles. These are located at specific energy levels, e.g., at 5.90, 5.35, and 5.13 eV, respectively, and originate mainly from interfacial defects; the other group contributes a relatively weak density of states, as indicated by the green arrows. The corresponding DOS is distributed over a wide range of energies, and originates in the exponentially decaying wave functions of the states on both sides of the barriers. As a common feature, both types of state extend into a larger fraction of the a-SiO_2 tunnel oxide layer.

Furthermore, a clear and deep band gap of 6.5 eV is found, located in the middle area of the c-Si/a-SiO_2:H/c-Si structure, which is indicative of an a-SiO_2 layer. This result is close to the 7.4–8.1 eV experimental band gap value for bulk a-SiO_2.[18] In addition, the band offset for the valence bands at the c-Si/a-SiO_2:H interface is estimated to be 2.2 eV, which is much larger than that of 0.25–0.45 eV at the c-Si/a-Si:H interface; meanwhile, the band offset for the conduction bands at the c-Si/a-SiO_2:H interface is 3.7 eV, which again is much larger than that of ∼0.15 eV at the c-Si/a-Si:H interface. Although the energy barriers at the interfaces are very high, the oxide layer does not prevent the majority of charge carrier transport across the barrier, as can be inferred from the fact that TOPCon solar cells are capable of exceeding an 82% of fill factor.[19] As such, the observed conductivity is attributed to tunneling transport through the ultra-thin oxide layer. To begin the process of shedding light on the dependence of transport characteristics on nanostructure configuration parameters, we first investigated the relationship between quantum conductance and the thickness of the tunnel oxide layer.

Figure 3 shows the quantum conductance results, computed for 0.6, 0.9, and 1.2 nm thick tunnel oxide layers, displayed together with the spatially integrated density of states. As expected, based on the exponential suppression of the tunneling probability with increasing barrier thickness, the c-Si/a-SiO_2:H/c-Si structure with a 0.6-nm-thick a-SiO_2 layer shows the highest conductivity. When the thickness of the oxide layer increases incrementally from 0.6 to 0.9 and 1.2 nm, the mobility gaps accordingly increase from 1.26 eV to 2.02 and 2.83 eV, respectively, resulting in an obvious decrement in terms of conductivity. The criterion for the determination of the mobility edges is set as a conductance of 10^{-4} $(2e^2/h)$. Unlike the

one-to-one correspondence between the band structure and the conductance spectrum for c-Si, in the c-Si/a-SiO_2:H/c-Si sandwich structures, the quantum conductance spectrum is greatly affected by the thickness of the tunnel oxide layer. The larger conductance for thinner barriers can be directly related to the larger DOS inside the barrier, as shown in Fig. 2. It should be noted that in tunnel-oxide passivated contact solar cells, although there is a strong intrinsic correlation between the DOS and conductivity, unlike crystalline silicon, there is no linear correspondence between them, due to the presence of local DOS in the passivation layer.

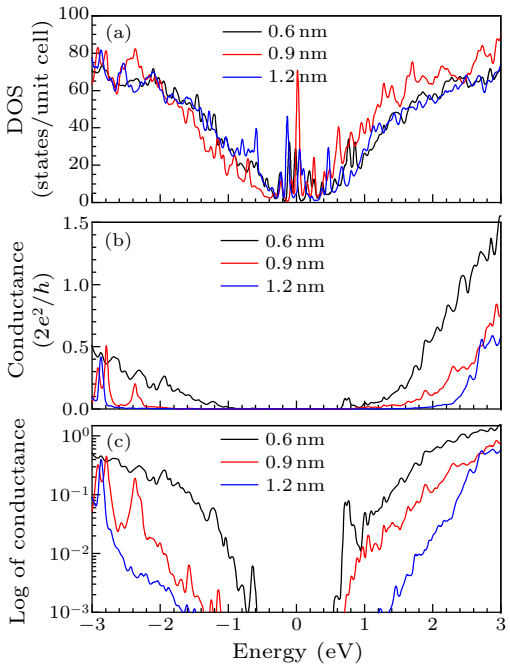

Fig. 3. (a) Spatially integrated density of states, (b) quantum conductance and (c) log scale of conductance for c-Si/a-SiO_2:H/c-Si with a tunnel oxide layer thickness of 0.6, 0.9, and 1.2 nm, respectively. The mobility gaps are 1.26, 2.02 and 2.83 eV. The criterion of the band edges is 10^{-4} $(2e^2/h)$.

Role of Passivation. One of the main factors limiting the efficiency of state-of-the-art silicon solar cells is the recombination of photogenerated electron-hole pairs that takes places at surfaces and interfaces. In this situation, surface passivation approaches can provide semiconductor/dielectric interfaces with very low recombination. To obtain a nanoscale picture of the impact of the passivation, we built two structures of c-Si/a-SiO_2/c-Si with and without H passivation. The corresponding LRDOS results are compared in Fig. 4. Unsaturated dangling bonds of Si atoms induce a large density of defect states at the interface, which can potentially form recombination centers. On the other hand, the presence of hydrogen significantly reduces the density of defect states at the interfaces.

To understand the role of dangling bond defects and their passivation in the tunneling transport process, the quantum conductance is computed, together with the density of states for both cases discussed above. As shown in Fig. 5(a), the analysis of the DOS reveals that the density of states around the Fermi level is higher when the interface is not passivated, which agrees well with the features in the LRDOS image. This new density of states originates from the silicon dangling bonds at the oxide-silicon interface. However, these new states do not contribute to the conductivity of the cell, as verified by the quantum conductance spectrum shown in Fig. 5(b).

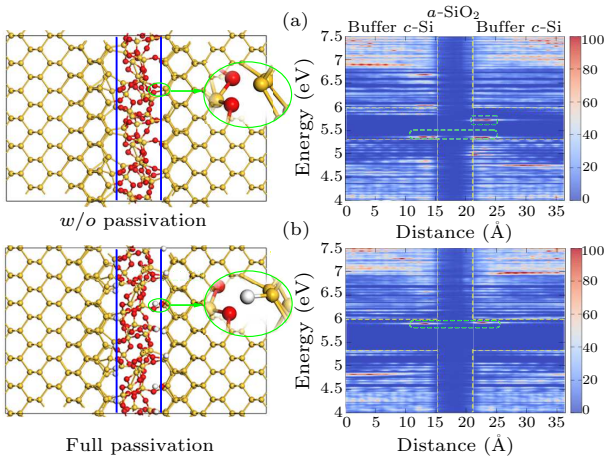

Fig. 4. Atomic structure and layer-resolved density of states (LRDOS) of c-Si/a-SiO_2/c-Si (a) without and (b) with full H-passivation at the interface between c-Si and a-SiO_2 layers, respectively. The thickness of the a-SiO_2 tunnel oxide layer is 0.6 nm. As a result of the passivation of dangling bond defects, localized surface states (dashed green circles in the LRDOS) are either removed or energetically shifted out of the detrimental mid-gap position.

In fact, we found that the conductivities in both the cases do not differ significantly. They both exhibit clear mobility gaps of ∼1.1 eV and ∼1.2 eV, respectively. These are higher than the electronic gap of 0.61 eV for c-Si, while much smaller than that of 7.4–8.1 eV for a-SiO_2 at the same theoretical level. Specifically, the conductivity of electrons without H passivation is slightly higher than that with full passivation, while that of the holes is similar. In other words, hydrogen passivation seems to suppress electron transport, widening the mobility gap. On the other hand, some tiny peaks are present in the gap of the transmission spectrum of the non-passivated sample, as marked by blue arrows in Figs. 5(b) and 5(c). These transmission channels are attributed to the density of states of the unpaired electrons, as they disappear upon saturation with hydrogen.

Impact of Stoichiometry. To compare the experimental and theoretical results, we took a TOPCon solar cell with a ∼1.2-nm-thick a-SiO_2 tunnel oxide layer as an example. In theory, it should exhibit very low conductivity, with a large mobility gap of 2.83 eV; experimentally, however, these samples continue to exhibit relatively high conductivity. This discrepancy indicates that direct tunneling may not be the only factor for the transport of charge carriers across real-

life tunnel oxide layers.

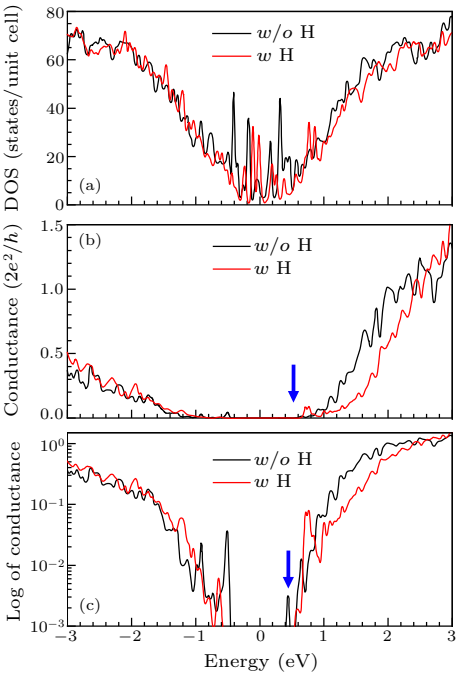

Fig. 5. (a) Integrated density of states, (b) quantum conductance and (c) log scale of conductance for c-Si/a-SiO_2/c-Si without (black line) and with (red line) H passivation. The thickness of the a-SiO_2 tunnel oxide layer is 0.6 nm. A notable effect of the hydrogen passivation is the removal of subgap transmission channels (lower arrow) and a moderate blue shift in the electron mobility edge.

Since the a-SiO_2 layer is grown wet-chemically in the experiment, a large number of O defects are usually induced. These defects are likely to alter the electronic properties of the tunnel oxide layer, with a potential modification to its conductivity. To understand the impact of O defects at the nanoscale level, we built a series of structures with an increasing number of O defects from 1, 2, 3, 4 to 5 in a-SiO_x, corresponding to stoichiometries where x = 1.97, 1.95, 1.92, 1.89 and 1.87, respectively. All the structures were fully optimized. The respective LRDOS is plotted in Fig. 6, reflecting the density of states corresponding to silicon atomic chains of different lengths formed in the a-SiO_x layer due to the missing O atoms. In fact, the formation of Si–Si bonds at the c-Si/a-SiO_2 interface has already been observed experimentally.[20]

To start with, we assume that there is only one O defect: either in the center of the a-SiO_x layer [Fig. 6(a)], or at the c-Si/a-SiO_2 interface [Fig. 6(b)]. In both the cases, Si–Si bonds are formed, taking the place of the original Si–O–Si bonds. This means that the O defects in the a-SiO_x layer will be self-healing after reconstruction. As a result, there are no additional defect states found in the gap of the a-SiO_x layer, which is confirmed by the LRDOS analysis. When there are two O defects, a short Si–Si–Si chain is formed, which is also energetically favorable in theory [Fig. 6(c)]. When three O defects are introduced, the length of the Si chain increases to ∼0.6 nm. A clearly distinguishable local density of states is formed in the gap of the a-SiO_x layer. For five O defects, the Si nanowire is long enough (∼1.0 nm) to bridge the neighboring sides. In this situation, a continuous density of gap states with similar energy is formed, crossing the mid-gap of the a-SiO_x layer in real space, as indicated by the green circles shown in Figs. 6(d), 6(e) and 6(f).

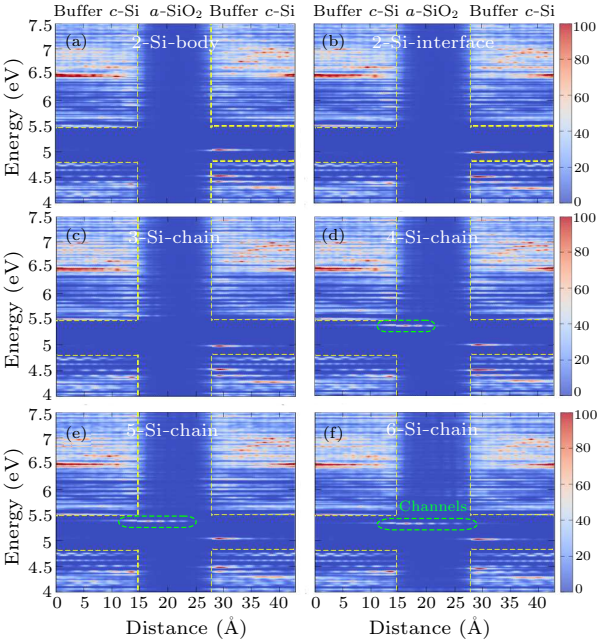

Fig. 6. Layer-resolved density of states of c-Si/a-SiO_x:H/c-Si: (a) two-silicon chain (single O vacancy), (c) three-silicon chain, (d) four-silicon chain, (e) five-silicon chain, and (f) six-silicon chain across the body of a-SiO_x. The thickness of a-SiO_x tunnel oxide layer is 1.2 nm. For more than five O vacancies (six-Si chains), new transmission channels appear in the gap, boosting the conductance of the oxide layer.

We then computed the conductivity of c-Si/a-SiO_x:H/c-Si with Si atomic nanowires of different lengths, as shown in Fig. 7. Insertion of O defects into the a-SiO_x layer increases the total density of states in the gap, due to the formation of Si–Si bonds. However, for a low number of O vacancies, these Si–Si bonds are isolated in the a-SiO_x layer, and do not contribute to the transport, as can be inferred from the conductance. When the length of the Si chain increases to ∼1.0 nm, conductivity is significantly enhanced, with a reduction of the mobility gap from ∼3 eV to 1.39 eV. For comparison, the mobility gap in the case of a 0.6-nm-thick a-SiO_x layer is computed to be ∼1.26 eV. We can clearly see the generative process of transmission channels when increasing the length of the Si chain, which we anticipate would enhance the total conductivity.

In order to address the origin of this conductivity enhancement with respect to the presence of long Si chains, we computed the average partial density of states of Si atoms in both the a-SiO_x layer and in the

∼1.0-nm-long Si chain. As shown in Fig. 7(c), the a-SiO_2 layer has a wide band gap of ∼6.5 eV, while the Si chain exhibits a much narrower energy gap. The density of states of the Si nanowire just fills the wide gap of the a-SiO_2 layer. As a result, new transmission channels are formed across the a-SiO_x.

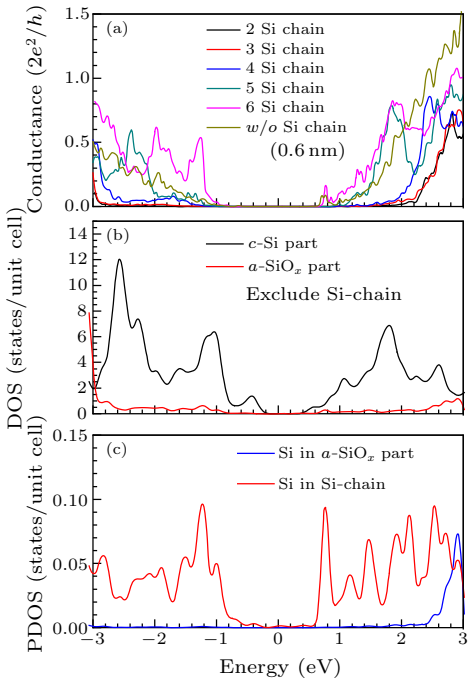

Fig. 7. (a) Quantum conductance for c-Si/a-SiO_x:H/c-Si configurations with Si chains of varying length. Again, the defining criterion of the mobility edges is 10^{-4} $(2e^2/h)$. (b) Total density of states of c-Si and a-SiO_x layers. (c) Average partial density of states of Si atoms in a-SiO_x layer and ∼1.0 nm Si nanowire. The thickness of the a-SiO_x tunnel oxide layer is 1.2 nm. For chains of more than five Si atoms (four O vacancies), conductance increases dramatically.

In summary, we have established a comprehensive simulation approach for the theoretical investigation of the electronic properties of tunnel oxide layers, based on first-principles electronic structure computations, combined with the non-equilibrium Green's function approach to quantum transport. When the thickness of the a-SiO_2 layer increases from 0.6 nm to 0.9 and then to 1.2 nm, conductivity is shown to decrease significantly, with an increment of mobility gaps from 1.26 eV to 2.02 and 2.83 eV, respectively. In addition, H passivation helps to repair the defects at the interfaces, but slightly lowers the conductivity for electrons, while hole transport remains unaffected. Furthermore, recombination of multiple oxygen vacancy defects in the a-SiO_x layer results in the formation of "monofilament pinholes" in the form of atomic Si nanowires, which dramatically increase conductivity. Our work has three points which are worth highlighting. Firstly, the model designed in this work is a promising and realistic one, which has great potential application in terms of future industrial development of silicon solar cells. Secondly, the structure size is very large as regarding first-principles research, and is thus more comparable to experimental research. Thirdly, three key points of discussion in this work, i.e., thickness, passivation, and oxygen vacancy, are also based on experimental phenomena, providing reliable theoretical simulations for experiments.

The authors gratefully acknowledge the computing time granted by the VSR commission on the supercomputer JURECA at Forschungszentrum Jülich.

References

[1] Feldmann F, Bivour M, Reichel C, Hermle M and Glunz S W 2014 *Sol. Energy Mater. Sol. Cells* **120** 270
[2] Richter A, Benick J, Feldmann F, Fell A, Hermle M and Glunz S W 2017 *Sol. Energy Mater. Sol. Cells* **173** 96
[3] Stodolny M K, Lenes M, Wu Y, Janssen G J M, Romijn I G, Luchies J R M *et al.* 2016 *Sol. Energy Mater. Sol. Cells* **158** 24
[4] Tao Y G, Upadhyaya V, Chen C W, Payne A, Chang E L, Upadhyaya A *et al.* 2016 *Prog. Photovoltaics* **24** 830
[5] Romer U, Peibst R, Ohrdes T, Lim B, Krugener J, Bugiel E *et al.* 2014 *Sol. Energy Mater. Sol. Cells* **131** 85
[6] Holman Z C, Descoeudres A, Barraud L, Fernandez F Z, Seif J P, Wolf S D *et al.* 2012 *IEEE J. Photovoltaics* **2** 7
[7] Peibst R, Romer U, Larionova Y, Rienacker M, Merkle A, Folchert N *et al.* 2016 *Sol. Energy Mater. Sol. Cells* **158** 60
[8] Kang J, Kim Y H, Bang J and Chang K J 2008 *Phys. Rev. B* **77** 195321
[9] Nardelli M B 1999 *Phys. Rev. B* **60** 7828
[10] Nardelli M B and Bernholc J 1999 *Phys. Rev. B* **60** R16338
[11] Kresse G and Hafner J 1993 *Phys. Rev. B* **48** 13115
[12] Kresse G and Furthmuller J 1996 *Phys. Rev. B* **54** 11169
[13] Giannozzi P, Baroni S, Bonini N, Calandra M, Car R, Cavazzoni C *et al.* 2009 *J. Phys.: Condens. Matter* **21** 395502
[14] Landauer R 1970 *Philos. Mag.* **21** 863
[15] Ferretti A, Calzolari A, Bonferroni B and Di Felice R 2007 *J. Phys.: Condens. Matter* **19** 036215
[16] Köhler M, Pomaska M, Lentz F, Finger F, Rau U and Ding K 2018 *ACS Appl. Mater. & Interfaces* **10** 14259
[17] Van de Walle C G and Martin R M 1987 *Phys. Rev. B* **35** 8154
[18] Nekrashevich S S and Gritsenko V A 2014 *Phys. Solid State* **56** 207
[19] Feldmann F, Bivour M, Reichel C, Hermle M and Glunz S W 2013 *28th European Photovoltaic Solar Energy Conference and Exhibition* (Paris, France, 30 September–4 October 2013) pp 988–992
[20] Yamashita Y, Asano A, Nishioka Y and Kobayashi H 1999 *Phys. Rev. B* **59** 15872

Supplementary Materials for "Quantum Transport across Amorphous-Crystalline Interfaces in Tunnel Oxide Passivated Contact Solar Cells: Direct versus Defect-Assisted Tunneling"

Feng Li(李峰)[1,2*], Weiyuan Duan(端伟元)[2], Manuel Pomaska[2], Malte Köhler[2], Kaining Ding(丁凯宁) [2], Yong Pu(普勇)[1]*, Urs Aeberhard[2], Uwe Rau[2]

[1] *College of Science, Nanjing University of Posts and Telecommunications, Nanjing, Jiangsu, 210023, China*

[2] *IEK-5 Photovoltaik, Forschungszentrum Jülich, 52425 Jülich, Germany.*

[*]Supported by National Natural Science Foundation of China (No. 61704083, 61874060), Natural Science Foundation of Jiangsu Province (No. BK20181388) and NUPTSF (No. NY219030). The authors gratefully acknowledge the computing time granted by the VSR commission on the supercomputer JURECA at Forschungszentrum Jülich.

%Email: lifeng@njupt.edu.cn; puyong@njupt.edu.cn

Theoretical details

The electronic ground states are described in terms of localized orbitals in the form of maximally-localized Wannier functions (MLWFs).[1] Due to the associated linear scaling of required computing time, the MLWFs method is especially effective in simulating a realistically sized device structure.[2-3] The Wannier-function Hamiltonian can be obtained by a Fourier transform from reciprocal space into real space for any arbitrary *k* point, as follows:

$$H_{mn}(k) = \sum_{R} e^{ik\cdot R} H_{mn}(R) \tag{1}$$

Then, the resulting Hamiltonian matrices can be diagonalized to find energy eigenvalues. Since the unitary transformations mix the energy bands at each *k* point, any arbitrary choice of states inside a prescribed window will affect the localization properties of WFs unless energy gaps effectively separate the manifold of interest from higher and lower bands. Thus, an additional disentanglement procedure is introduced to solve this problem,[4] by extracting the best possible manifold of a given dimension from the states falling in a predefined energy window.

Using the Hamiltonian matrices calculated in the last step, the zero-temperature conductance spectrum is computed using the Landauer formula[5] as implemented in the WanT code[6]:

$$C = \frac{2e^2}{h} T(E_f) \tag{2}$$

where C is the conductance, T is the transmission function, and E_f is the Fermi energy. $2e^2/h$ is the quantum unit of conductance, where h is the Planck′s constant and e is the electronic charge. It represents the probability that an electron injects at one end and transmits to the other end.

The transmission function is expressed in terms of the Green's function of the conductor and

the couplings of the conductor to the leads using the Fisher and Lee formula[7]:

$$T = T_r[\Gamma_L G^r \Gamma_R G^a] \tag{3}$$

Here, $G^r$and G^a are the retarded and advanced Green's functions of the conductor. Γ_L and Γ_R are the functions that describe the coupling of the conductor to the leads. There are two modes for computing the transmittance: two-terminal mode the bulk mode. For the two-terminal mode, all of the information contained in the Hamiltonian is needed, including the on-site Hamiltonian of the conductor (H00_C) and of left/right leads (H00_L and H00_R), the hopping Hamiltonian of left/right leads (H01_L and H01_R), and the coupling between lead and conductor (H_LC and H_CR); while for the bulk mode, only H00_C and H_CR are required.

Finally, the total conductance can be computed. Since all the details of the electronic structure are included in the Hamiltonian matrix, all of the density state for the tunneling transport are automatically considered when computing the transmission spectrum. This integrated method allows for a direct link between the nature of the chemical bonds and the electronic transport properties of the device, providing insight into the mechanisms that govern electron flow at the nanoscale.

Crystalline silicon. We first consider the structural, electronic and transport properties of ideal bulk *c*–Si in order to verify the correctness of the integrated simulation approach. A unit cell containing 8 silicon atoms is used, with a lattice constant of 5.46 Å. The optimized Si–Si bond is 2.35 Å, matching well with the experimental result of ~2.35 Å. The computed electronic band structure of *c*–Si is shown in Fig. S1.

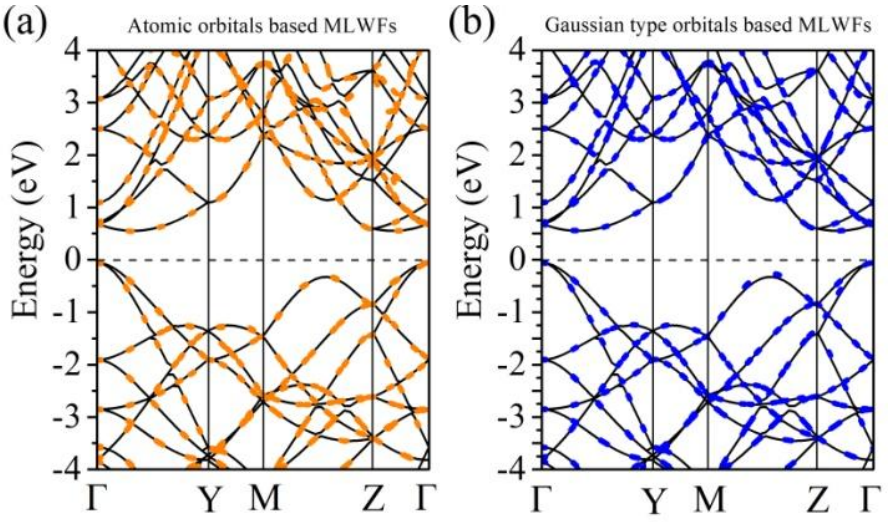

Fig. S1. Band structure of bulk crystalline silicon. The interpolated Wannier band structure based on a set of (a) atomic orbitals, and (b) one-, two-Gaussian type orbitals are depicted in orange and blue dots, respectively. The black lines represent the first-principles band structure based on the Bloch states. The Fermi level is set at 0 eV, indicated as a black dashed line. All the results are computed at the PBE level.

To achieve a linear scaling of required computing time, the electron Bloch wavefunctions, obtained from the *ab initio* calculation, are translated into the MLWF forms through a unitary transformation. The band structure is calculated based on the Hamiltonian as represented in a basis

of MLWFs. Since the choice of a suitable set of Wannier functions is the key to construct the accurate Hamiltonian matrix, we applied two widely used sets of Wannier functions as initial functions: a set of atomic orbitals and a set of one-, two- Gaussian type orbitals. The results are compared and plotted in Fig. S1ab as orange and blue dots, respectively. To check the accuracy of the MLWFs method, the electronic band structure of *c*–Si based on Bloch wavefunctions is also computed and displayed as solid black lines. The chosen set of MLWFs reproduces the band structure of *c*–Si very well. It exhibits a clear indirect band gap of 0.60 eV, which is very close to the DFT result of 0.61 eV. This result proves that the MLWFs method conserves the accuracy of the first-principles electronic structure calculations, confirming the reliability of the integrated method used in this work. Since the accuracy is very similar for atomic orbitals and Gaussian-type orbitals, while the former costs ~30 % less memory than the latter, we thus used atomic orbitals as initial Wannier functions for MLWFs in all of the computations.

We then calculated the conductance for bulk *c*–Si by bulk model. The transport is computed by interpolating the in-plane *k* points as integrated into the WanT codes. We found that *c*–Si has a clear transmission gap of 0.62 eV (Fig. S2b). This value agrees well with the computed electrical band gap of 0.61 eV, which is also consistent with the result of the density of states (Fig. S2a). The quantum conductance is a constant proportional to the number of transmitting channels available for charge mobility, which are equal to the number of bands at the same energy. This result indicates a one-to-one correspondence between the band structure and the quantum conductance spectrum for *c*–Si. On the other hand, for the amorphous-crystalline interfaces, the conductance will display a large complex that is related to the channel DOS and contact DOS, which is discussed in the next section.

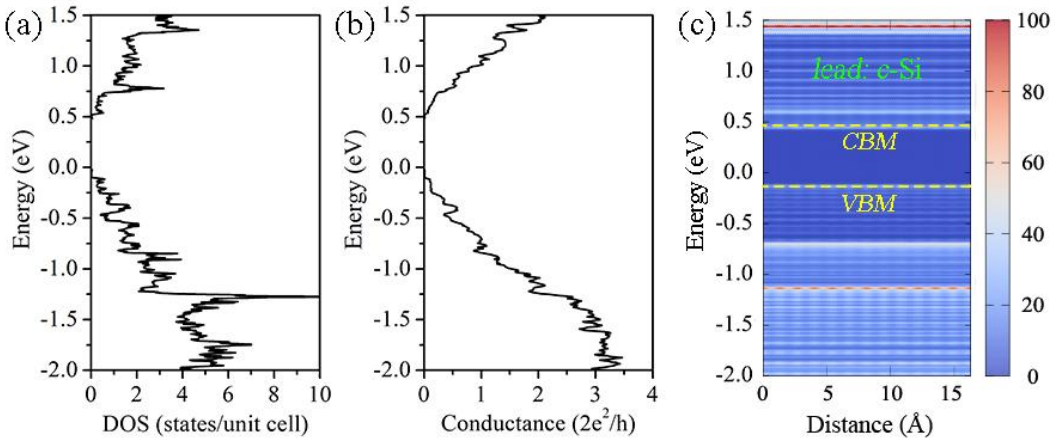

Fig. S2. (a) Spatially integrated density of states, (b) quantum conductance and (c) layer-resolved density of states of *c*–Si along the [001] direction. The valence band maximum and conduction band minimum are highlighted in dashed yellow lines.

Since only the bands around the gap will effectively be involved in the electronic transport, we examine the layer-resolved density of states (LRDOS) of *c*–Si to determine the band edges around the Fermi level. A downshift of 6 eV is applied in Fig. S2c in order to match the electronic band structure. In this condition, the valence band maximum (VBM) is computed to be at –0.10 eV and the conduction band minimum (CBM) is at 0.53 eV. In Fig. S2c, the band edges are highlighted in dashed yellow lines. We found that the gap between the VBM and CBM in LRDOS is ~0.63 eV, which is in good agreement with the transmission gap of 0.62 eV.

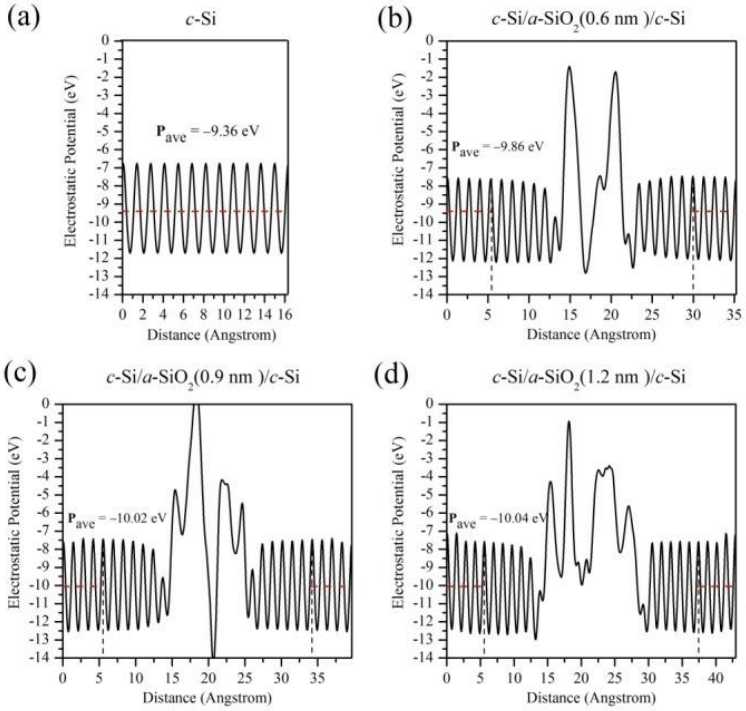

Fig. S3. Electrostatic potential of (a) the *c*–Si lead and the buffer layer in the *c*–Si/*a*–SiO_2/*c*–Si sandwich structures with thicknesses of (b) 0.6, (c) 0.9 and (c) 1.2 nm *a*–SiO_2 tunnel oxide layer.

Reference

(1) Marzari, N.; Mostofi, A. A.; Yates, J. R.; Souza, I.; Vanderbilt, D., Maximally Localized Wannier Functions: Theory and Applications. *Rev. Mod. Phys.* **2012**, *84*, 1419-1475.

(2) Calzolari, A.; Marzari, N.; Souza, I.; Nardelli, M. B., Ab Initio Transport Properties of Nanostructures from Maximally Localized Wannier Functions. *Phys. Rev. B* **2004**, *69*, 035108.

(3) Want Code by A. Ferretti, B. Bonferroni, A. Calzolari, and M. Buongiorno Nardelli, Http://Www.Wannier-Transport.Org.

(4) Souza, I.; Marzari, N.; Vanderbilt, D., Maximally Localized Wannier Functions for Entangled Energy Bands. *Phys. Rev. B* **2001**, *65*, 035109.

(5) Landauer, R., Electrical Resistance of Disordered One-Dimensional Lattices. *Philos. Mag.* **1970**, *21*, 863-867.

(6) Ferretti, A.; Calzolari, A.; Bonferroni, B.; Di Felice, R., Maximally Localized Wannier Functions Constructed from Projector-Augmented Waves or Ultrasoft Pseudopotentials. *J Phys-Condens Mat* **2007**, *19*.

(7) Fisher, D. S.; Lee, P. A., Relation between Conductivity and Transmission Matrix. *Phys. Rev. B* **1981**, *23*, 6851-6854.